

Déjà View: Looping Transformers for Multi-View 3D Reconstruction

Alessandro Burzio^{*1,2} Tobias Fischer^{*1,4} Sven Ellein^{1,3} Qunjie Zhou¹
 Riccardo de Lutio¹ Jiawei Ren¹ Jiahui Huang¹ Shengyu Huang¹
 Marc Pollefeys⁴ Laura Leal-Taixé¹ Zan Gojic^{†1} Haithem Turki^{†1}

¹NVIDIA ²University of Modena and Reggio Emilia, AImageLab
³University of Toronto, Vector Institute ⁴ETH Zürich
^{*}Equal contribution [†]Equal supervision

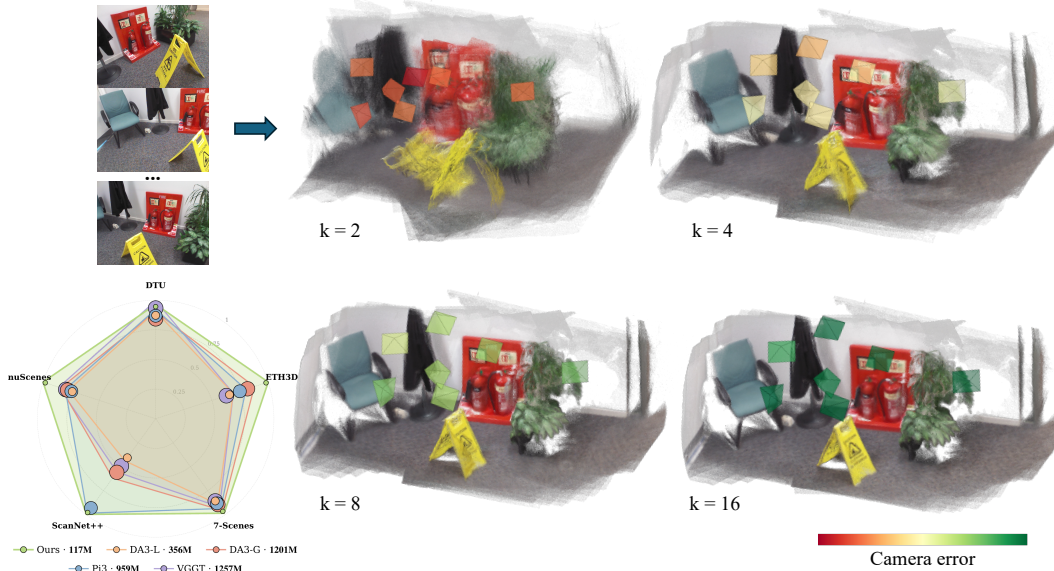


Figure 1: **Déjà View**. Given multiple input views (**top-left**), DéjàView reconstructs camera poses and consistent depth by repeatedly applying the *same* transformer block, with the number of refinement steps K exposed as an inference-time compute knob. Decoding the intermediate state of a single $K=16$ forward pass at iterations $k \in \{2, 4, 8, 16\}$ shows progressively sharper geometry and more accurate camera poses (**right**; frustums are colored by per-camera error). Across five benchmarks (**bottom-left**), DéjàView matches or surpasses much larger feed-forward baselines at a small fraction of their parameter count (dot area).

Abstract

Recent feed-forward 3D reconstruction transformers have scaled to over a billion parameters, following the broader trend of increasing model capacity in computer vision. Yet emerging evidence suggests that contiguous transformer layers often behave like repeated applications of similar operations [Jacobs et al., 2026], and multi-view reconstruction transformers refine their predictions progressively across decoder depth [Starý et al., 2025]. We posit that model depth partially buys iteration, paid for inefficiently in unique parameters, and instead make that iteration explicit

in architecture. Our model, DéjàView, applies a single looped transformer block recurrently to per-view features for K refinement steps. Trained once, it exposes K as an inference-time compute knob, matching or outperforming substantially larger feed-forward baselines across five reconstruction benchmarks spanning indoor, outdoor, object-centric, and driving scenes, while using a fraction of their parameters and comparable or lower compute. Importantly, the same looped block formulation outperforms an otherwise identical variant with independent per-step parameters under matched training data and compute, suggesting that explicit iteration is not merely a compute-efficient substitute for capacity but a stronger inductive bias for multi-view 3D reconstruction. We release code and model on our project page <https://research.nvidia.com/labs/dvl/projects/dvlt/>.

1 Introduction

Recovering 3D structure from images has traditionally relied on a Structure-from-Motion (SfM) pipeline [Schönberger and Frahm, 2016, Pan et al., 2024]. These systems decompose reconstruction into feature extraction and matching, pose estimation, triangulation, and global bundle adjustment, yielding an inherently iterative process that alternates between registering new views and re-adjusting previous estimates.

More recently, feed-forward methods [Wang et al., 2024, Leroy et al., 2024, Wang et al., 2025, Lin et al., 2025, Wang et al., 2025b, Keetha et al., 2026, Wang et al., 2026] have replaced this pipeline with an end-to-end transformer that regresses 3D geometry from images in a single forward pass. Their gains, in line with the broader trend in computer vision [Dosovitskiy et al., 2021, Zhai et al., 2022, Radford et al., 2021, Oquab et al., 2024, Kirillov et al., 2023], have largely been driven by scaling model capacity through backbone depth and width [Lin et al., 2025].

Yet iteration may not have disappeared at all — it may simply have been absorbed into network depth. Jacobs et al. [2026] show that for some applications the L layers of a Vision Transformer (ViT) can be replaced with $K \ll L$ recurrent applications of a looped block with little loss in accuracy. Starý et al. [2025] further probe the decoder of DUST3R [Wang et al., 2024] layer-by-layer and find that its pointmap predictions are themselves iteratively refined across depth, despite the layers being independently parameterized.

Together, these observations suggest that part of the benefit of depth in modern reconstruction transformers arises from implicit iterative refinement, at the cost of redundant layer-specific parameters.

We therefore make this iterative process explicit in the architecture, rather than relying on model depth to realize it implicitly. Starting from per-view DINOv2 [Oquab et al., 2024] features, we apply a single looped transformer block recurrently for K refinement steps. By sampling K from $[K_{\min}, K_{\max}]$ during training, a single checkpoint exposes K as an inference-time compute knob without retraining. Analyzing the trained recurrence reveals that it does not converge to a fixed point. Instead, each step progressively aligns the state’s direction toward its endpoint, a regime we call *directional refinement*.

The resulting model, DéjàView, matches or surpasses much larger feed-forward baselines across five reconstruction benchmarks spanning indoor, outdoor, object-centric, and driving scenes, at a small fraction of their parameters and comparable or lower compute. Importantly, we show that our looping formulation with shared weights significantly outperforms an otherwise identical variant with independent per-step parameters under the same training data and compute budget. We take this as evidence that iterative refinement with shared weights is a viable alternative to parameter scaling for 3D reconstruction.

We summarize our contributions as follows:

- DéjàView, a looping transformer for multi-view 3D reconstruction that applies a single shared block recurrently to a DINOv2-initialized state, with each step conditioned on a continuous time interval.
- A variable- K training recipe in which the step count is sampled per batch from $[K_{\min}, K_{\max}]$, yielding a single checkpoint that exposes compute as an inference-time knob.
- State-of-the-art reconstruction quality across five challenging benchmarks, at a small fraction of the parameters and comparable or lower compute.

2 Related Work

Our work draws on several lines of research spanning 3D reconstruction, iterative refinement for geometry estimation, and weight-tied network design.

Multi-view 3D reconstruction. Classical Structure-from-Motion [Schönberger and Frahm, 2016, Pan et al., 2024] recovers geometry through feature matching, pose estimation, and bundle adjustment, but is brittle on in-the-wild scenes with weak texture or dynamic content. Learning-based methods have progressively replaced individual stages of this pipeline, from multi-view stereo [Yao et al., 2018] to fully end-to-end systems. DUS_t3R [Wang et al., 2024] and MAS_t3R [Leroy et al., 2024] regress pairwise pointmaps from a CroCo-pretrained [Weinzaepfel et al., 2022] backbone, while VGGT [Wang et al., 2025] and concurrent methods [Wang et al., 2025b, Lin et al., 2025, Keetha et al., 2026, Wang et al., 2026] process all views jointly through a DINOv2 [Oquab et al., 2024]-based transformer, with extensions to incremental capture [Wang and Agapito, 2025, Wang* et al., 2025], large view counts [Yang et al., 2025, Elflein et al., 2026], pose-free Gaussian splatting [Ye et al., 2025], multiple dense geometric quantities [Fang et al., 2026] and dynamic scenes [Zhang et al., 2025, Sucar et al., 2026, Luo et al., 2026]. All of these systems use a fixed-depth architecture with many unique parameters. We instead frame multi-view reconstruction as iterative refinement, matching the quality of these deeper feed-forward networks at a fraction of the parameter count while exposing the number of refinement steps as an inference-time compute knob.

Iterative refinement. RAFT [Teed and Deng, 2020] introduced GRU-based iterative refinement of a per-pixel flow field, an idiom since broadly applied to stereo matching [Lipson et al., 2021], visual SLAM [Teed and Deng, 2021, Huang et al., 2025], and multi-view stereo [Wang et al., 2022]: in each case, a lightweight recurrent updater iteratively refines geometry on top of a fixed feature backbone. iLRM [Kang et al., 2026] extends iterative refinement to feed-forward 3D Gaussian splatting by treating successive (unshared) transformer layers as optimization steps over a scene representation decoupled from the input views. Unlike RAFT-style designs, where a lightweight recurrent updater iterates on a precomputed correspondence volume from a fixed feature backbone, our recurrence interleaves cross-view reasoning and refinement: each step is a full transformer block with frame and global attention, applied to per-view tokens initialized from a DINOv2 patch encoder. Cross-view reasoning and refinement therefore occur within the same repeated computation, rather than being assigned to separate stages. Unlike iLRM, the block is shared across all K steps and refines the per-view tokens themselves rather than a decoupled scene state.

Weight-tied transformers. Applying a shared transformer block repeatedly across depth dates back to Universal Transformers [Dehghani et al., 2019], which paired weight tying with adaptive halting [Graves, 2017], and ALBERT [Lan et al., 2020], which showed that cross-layer parameter sharing yields competitive language models at a fraction of the parameters. Follow-ups have explored weight-tied recurrence in language modeling [Hutchins et al., 2022, Yang et al., 2024, Saunshi et al., 2025, Geiping et al., 2025] and learned-iteration in algorithmic tasks where networks trained for K steps extrapolate to $K' > K$ at test time [Schwarzschild et al., 2021, Bansal et al., 2022]. RAPTOR [Jacobs et al., 2026] showed that trained Vision Transformers admit an analogous structure: the layers can be faithfully approximated by a much smaller set of looped blocks, fit via post-hoc distillation against the original network. We adopt RAPTOR’s gated block design but apply it differently. Rather than distilling a pretrained network into a looped form, we train a single shared block end-to-end on a 3D reconstruction task loss, with no teacher network and no distillation targets, and surpass an otherwise identical decoupled-parameters variant (Table 4) under matched training data and compute.

3 Method

3.1 Problem setup

Given a set of V input images $\{\mathbf{I}_i\}_{i=1}^V$ with $\mathbf{I}_i \in \mathbb{R}^{H \times W \times 3}$, our goal is to recover the underlying 3D scene geometry, expressed in the coordinate frame of the first view. We adopt a depth-ray representation: for each image \mathbf{I}_i , the model predicts a per-pixel depth map $\mathbf{D}_i \in \mathbb{R}^{H \times W}$ and a dense ray map $\mathbf{R}_i \in \mathbb{R}^{H \times W \times 6}$. Each pixel of the ray map encodes a 3D origin $\mathbf{R}^o \in \mathbb{R}^3$ and an unnormalized direction $\mathbf{R}^d \in \mathbb{R}^3$, so that a 3D point in world coordinates is obtained as

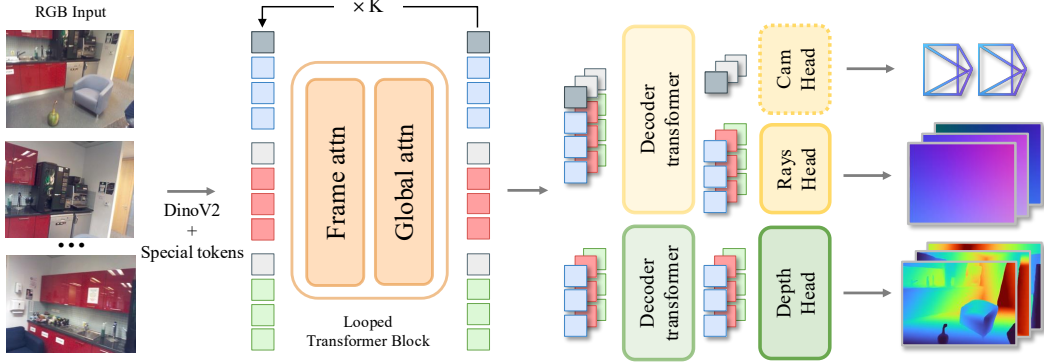


Figure 2: **Method overview.** V input images are encoded by a shared DINOv2 [Oquab et al., 2024] backbone. A single looped transformer block with frame-wise and global attention sub-blocks is then applied recurrently to the resulting tokens for K steps, with K sampled per batch from $[K_{\min}, K_{\max}]$ during training. Two heads decode the final tokens into per-view depth and ray predictions.

$\mathbf{X} = \mathbf{R}^o + \mathbf{D}(u, v) \cdot \mathbf{R}^d$. Per-view camera-to-world rotations $\mathbf{R}_i \in SO(3)$, translations $\mathbf{t}_i \in \mathbb{R}^3$, and intrinsic matrices $\mathbf{K}_i \in \mathbb{R}^{3 \times 3}$ are recovered from the predicted ray maps following Lin et al. [2025].

3.2 Hypothesis

Two recent analyses motivate our approach. First, Jacobs et al. [2026] show via post-hoc distillation that the L layers of a trained ViT can be accurately approximated by a few looped blocks. Second, Starý et al. [2025] probe DUST3R [Wang et al., 2024] layer by layer and show that its predicted pointmaps progressively refine across decoder depth, revealing iterative refinement of geometry inside multi-view transformers even though their layers do not share weights.

We hypothesize that this structure can be made explicit by applying a looped block to an evolving state, and that the resulting recurrence performs *directional refinement* of the state, where the direction of \mathbf{z}_k converges to the endpoint direction over the trained step range (Sections 3.4 and 4.2). In contrast to task-space iterative refinement methods such as RAFT [Teed and Deng, 2020, Lipson et al., 2021], which decode after every step and apply a sequence loss on the output, we refine an internal state with a looped block and supervise only at the final step. This avoids running the decoder and computing a loss at every intermediate step, sparing $(K-1)$ decoder forward and backward passes per training iteration.

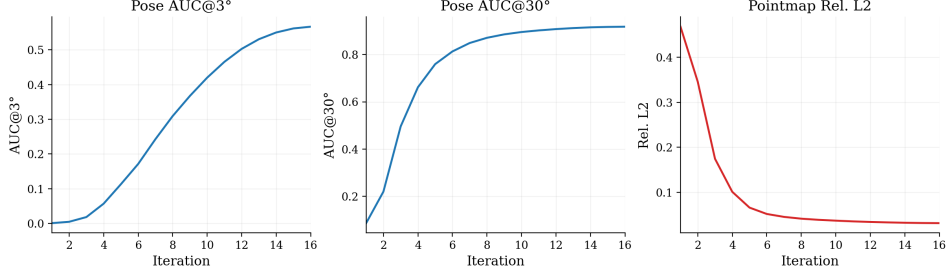
We model the recurrence as a time-conditioned discrete update over the partition $0 = t_0 < t_1 < \dots < t_K = 1$ of the unit interval:

$$\mathbf{z}_{k+1} = f_{\theta}(\mathbf{z}_k, t_k, t_{k+1}), \quad (1)$$

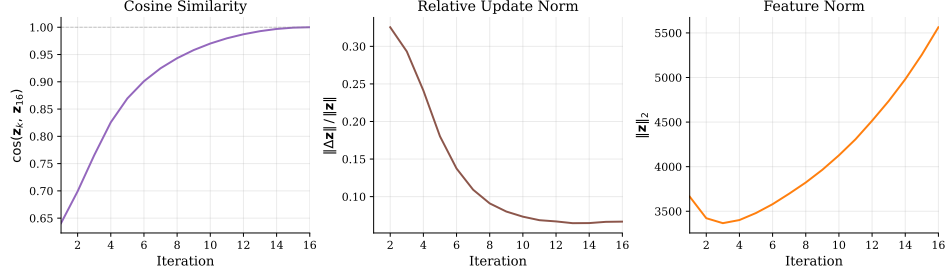
where f_{θ} is a looped block conditioned on the continuous time interval (t_k, t_{k+1}) . Conditioning on continuous time, rather than on a discrete step index as in prior weight-tied transformers [Dehghani et al., 2019], decouples the block from any specific value of K and lets a single set of weights cover a range of step counts at inference. Section 3.4 instantiates f_{θ} as a shared transformer block with frame and global attention.

3.3 Architecture

Patch encoder and tokens. We initialize the per-view state \mathbf{z}_0 from a pretrained DINOv2 [Oquab et al., 2024] encoder, which maps each input image to an $\frac{H}{P} \times \frac{W}{P}$ grid of patch tokens. We prepend a per-view copy of R learnable register tokens [Darcet et al., 2024] and of a learnable camera token to each view’s token sequence, with the underlying parameters tied across views. The camera token uses two parameter sets: one for the reference (first) view, and one tied across all other views. We encode patch positions with 2D rotary position embeddings [Heo et al., 2024] and assign special tokens a sentinel position outside the patch grid. We then apply a looped transformer block K times to \mathbf{z}_0 , with K randomly sampled per training batch (Section 3.4), yielding the final state \mathbf{z}_K passed to the decoder heads.



(a) **Task quality across recurrent iterations.** Decoding the residual stream \mathbf{z}_k at every iteration $k \in \{1, \dots, 16\}$ yields monotone improvement of pose and pointmap metrics across the trained step range.



(b) **Residual-stream convergence.** *Left:* cosine similarity between \mathbf{z}_k and the final \mathbf{z}_{16} . *Middle:* relative update norm $\|\Delta\mathbf{z}_k\|/\|\mathbf{z}_k\|$. *Right:* feature norm $\|\mathbf{z}_k\|_2$.

Figure 3: **Iterative refinement of the residual stream.** Per-iteration analysis of DéjàView’s recurrent block, averaged across the five benchmarks of Tables 1 and 2. Task quality improves monotonically with the iteration count (**top**). The recurrence does not contract to a fixed point in feature space (the state norm grows) but its direction stabilizes, with cosine similarity to the final state approaching 1 and the relative update norm decaying by roughly $5\times$ (**bottom**). The decoder’s input LayerNorm absorbs the norm growth, so the decoded representation effectively converges in direction.

Decoder heads. We pass \mathbf{z}_K through two parallel decoder branches, each comprising a shallow transformer followed by an output head. Each decoder transformer uses the same pre-norm Attn + MLP block design as the shared recurrent block (Section 3.4), but without LayerScale. The ray decoder uses a linear pixel-shuffle head to produce the per-pixel ray map $\mathbf{R}_\theta \in \mathbb{R}^{H \times W \times 6}$. The depth decoder uses a convolutional depth head following Wang et al. [2025a] to avoid block artifacts at patch boundaries (Section B), and produces the depth map $\mathbf{D}_\theta \in \mathbb{R}^{H \times W}$ and a depth confidence map $c_D \in \mathbb{R}^{H \times W}$. Following Lin et al. [2025], we additionally include a camera MLP head that decodes a tuple $\mathbf{c}_\theta = (\mathbf{t}_\theta, \mathbf{q}_\theta, \mathbf{f}_\theta) \in \mathbb{R}^3 \times \mathbb{S}^3 \times \mathbb{R}^2$, comprising translation, unit rotation quaternion, and field of view, from the per-view camera tokens at the output of the ray decoder (Section 3.5). It provides a faster alternative to the rays-derived recovery of Section 3.1, which remains our default at inference. We obtain world points analytically as $\mathbf{X}_\theta = \mathbf{R}_\theta^o + \mathbf{D}_\theta \cdot \mathbf{R}_\theta^d$.

3.4 Looped Block

Block design. The looped block consists of two attention sub-blocks applied in sequence, following the alternating frame/global design of VGGT [Wang et al., 2025]. The first is a frame attention that processes each view independently with 2D rotary position embeddings. The second is a global attention that operates over the joint sequence of all tokens across all views. Each sub-block uses a standard pre-norm Attn + MLP design with LayerScale [Touvron et al., 2021].

We condition the block on the time interval (t_k, t_{k+1}) . Three channel-wise scale vectors $(\mathbf{s}_{\text{attn}}, \mathbf{s}_{\text{mlp}}, \mathbf{s}_{\text{out}})$ control the block update:

$$\begin{aligned}
 \mathbf{z}' &= \mathbf{z}_k + \mathbf{s}_{\text{attn}} \odot \text{LS}_1(\text{Attn}(\text{LN}_1(\mathbf{z}_k))), \\
 \mathbf{z}'' &= \mathbf{z}' + \mathbf{s}_{\text{mlp}} \odot \text{LS}_2(\text{MLP}(\text{LN}_2(\mathbf{z}'))), \\
 \mathbf{z}_{k+1} &= \mathbf{s}_{\text{out}} \odot \mathbf{z}'',
 \end{aligned} \tag{2}$$

where LN is layer normalization, LS is LayerScale, and \odot is channel-wise multiplication broadcast over the sequence dimension. We compute the scales via a zero-initialized MLP such that $\mathbf{s} = \mathbf{1} + \text{MLP}(\gamma(t_k, t_{k+1}))$, where γ concatenates the sinusoidal embeddings of t_k and t_{k+1} . We ablate simpler variants of this block (no \mathbf{s}_{out} , no time conditioning, and untied per-step blocks) in Section 4.2.

Variable step count. We train a single set of weights to serve as a K -elastic family: the same block supports a range of step counts K at inference, exposed as a compute knob. Specifically, we sample $K \sim \text{Beta}(\alpha, \beta)$ per batch, scaled and rounded into $[K_{\min}, K_{\max}]$, and apply the block K times along the uniform partition $0 = t_0 < t_1 < \dots < t_K = 1$ with $t_k = k/K$, where the application from \mathbf{z}_k to \mathbf{z}_{k+1} is conditioned on the interval (t_k, t_{k+1}) . At inference, we run the block on a uniform grid of K_{inf} steps; varying K_{inf} trades compute for accuracy within the trained range $[K_{\min}, K_{\max}]$, with degradation observed when K_{inf} is pushed substantially outside it (Section 4.2, Section D).

Directional refinement. Unlike deep equilibrium networks [Bai et al., 2019], our recurrence does not converge to a fixed point in feature space. Instead, the state norm $\|\mathbf{z}_k\|$ grows monotonically with k . However, two empirical signatures characterize its dynamics within the trained step range (Figure 3). First, $\cos(\mathbf{z}_k, \mathbf{z}_K)$ rises monotonically toward 1 as $k \rightarrow K$, which means that each step moves the state closer in direction to the endpoint. Second, the relative update magnitude $\|\Delta\mathbf{z}_k\|/\|\mathbf{z}_k\|$ decays from ~ 0.5 at the first step to ~ 0.1 at the last, indicating a genuine slowdown of motion rather than a constant rescaling. Because each decoder branch is pre-norm (Section 3.3), the LayerNorm at the start of its first transformer block absorbs the component of $\Delta\mathbf{z}_k$ parallel to \mathbf{z}_k that drives the norm growth, and the decoded representation effectively converges in direction. We refer to this behavior as *directional refinement*, distinct from RAFT-style task-space refinement [Teed and Deng, 2020] that operates on the output and contracts in absolute magnitude.

3.5 Training

Losses. We supervise the model directly on the predicted geometry with five complementary loss terms covering depth, rays, world points, and camera parameters. Following DUST3R [Wang et al., 2024], predictions and ground truth are independently normalized prior to loss computation: given valid 3D points $\{\mathbf{X}_j\}_{j \in \Omega}$, we define the inverse normalization scale

$$s = \left(\frac{1}{|\Omega|} \sum_{j \in \Omega} \|\mathbf{X}_j\|_2 \right)^{-1}, \quad (3)$$

computed separately for the predicted (\hat{s}) and ground-truth (\bar{s}) point clouds. The per-sample training loss is then:

$$\begin{aligned} \mathcal{L} = & \|\hat{s} \mathbf{D}_\theta - \bar{s} \mathbf{D}\|_2 + \mathcal{L}_{\text{grad}}(\hat{s} \mathbf{D}_\theta, \bar{s} \mathbf{D}) + \|\hat{s} \mathbf{R}_\theta - \bar{s} \mathbf{R}\|_1 \\ & + \|\hat{s} \mathbf{X}_\theta - \bar{s} \mathbf{X}\|_2 + \mathcal{L}_{\text{cam}}(\mathbf{c}_\theta, \mathbf{c}), \end{aligned} \quad (4)$$

where $\mathbf{X}_\theta = \mathbf{R}_\theta^o + \mathbf{D}_\theta \cdot \mathbf{R}_\theta^d$ is the analytically derived predicted point cloud, $\mathcal{L}_{\text{grad}}$ is a multi-scale ℓ_1 loss on horizontal and vertical depth gradients [Hu et al., 2019, Lin et al., 2025], and \mathcal{L}_{cam} decomposes into separately weighted ℓ_1 terms on the translation, rotation, and field-of-view components of \mathbf{c}_θ . The pointmap term ties the depth and ray heads through a joint geometric signal.

Optimization. Training proceeds in two stages. The first stage trains the model end-to-end with all loss terms, using plain ℓ_2 regression on the depth and pointmap terms and a linear pixel-shuffle depth head. The second stage swaps in the convolutional depth head described in Section 3.3 and finetunes the depth decoder while freezing all other parameters. The ray and camera losses are disabled in the second stage. The depth term applies DUST3R-style confidence weighting [Wang et al., 2024], $\mathcal{L}_{\text{unc}}(c, \mathbf{a}, \mathbf{b}) = c\|\mathbf{a} - \mathbf{b}\|_2 - \lambda_c \log c$, parameterized by the predicted per-pixel uncertainty c_{D} , while the pointmap term remains plain ℓ_2 on the analytically derived points.

4 Experiments

Implementation. We implement our method in PyTorch [Paszke et al., 2019] and train on 128 H100 GPUs with $V \in [2, 18]$ views per scene at 504-pixel longest-edge resolution. Each training step uses up to 4,608 images and a fixed tokens budget ($\approx 2.5\text{M}$ tokens). We use a DINOv2 ViT-B encoder with embedding dimension 768, patch size $P=14$, and $R=4$ register tokens. The ray and depth decoders

Table 1: **Pointmap accuracy.** Relative ℓ_2 distance (**Rel. L2** \downarrow) and inlier ratio (**IR** \uparrow) on the global pointmap after a Sim(3) alignment to the ground truth, across five benchmarks. The **best**, **second**, and **third** ranked results are highlighted. VGGT- Ω [Wang et al., 2026] is concurrent work, reported here for completeness.

Method	DTU		ETH3D		7-Scenes		ScanNet++		nuScenes	
	Rel. L2	IR	Rel. L2	IR	Rel. L2	IR	Rel. L2	IR	Rel. L2	IR
MASt3R [Leroy et al., 2024]	0.011	94.9	0.340	29.1	0.076	41.7	0.251	14.5	0.360	11.4
MASt3R-SfM [Duisterhof et al., 2024]	0.009	96.9	0.095	54.1	0.051	64.7	0.042	69.7	0.311	18.4
MapAnything [Keetha et al., 2026]	0.014	95.2	0.227	40.6	0.044	67.9	0.019	89.2	0.089	51.9
Pi3 [Wang et al., 2025b]	0.009	97.3	0.034	66.8	0.032	77.8	0.014	94.3	0.078	51.0
VGGT [Wang et al., 2025]	0.010	95.8	0.053	52.6	0.042	70.8	0.034	68.4	0.081	42.3
VGGT- Ω -1B [Wang et al., 2026]	0.009	97.2	0.024	78.6	0.039	65.3	0.032	70.6	0.055	62.3
DA3-L [Lin et al., 2025]	0.010	97.1	0.211	49.9	0.039	69.6	0.051	48.1	0.141	27.0
DA3-G [Lin et al., 2025]	0.010	97.1	0.129	64.7	0.037	71.1	0.041	57.8	0.080	42.0
Ours	0.009	97.1	0.026	78.3	0.035	74.2	0.015	93.3	0.067	58.5

Table 2: **Camera pose accuracy.** Area under the cumulative pose-error curve at 3° (**AUC@3** \uparrow) and 30° (**AUC@30** \uparrow), across five benchmarks. VGGT- Ω [Wang et al., 2026] is concurrent work, reported here for completeness. DéjàView ranks first or second on nine of ten cells and is in the top three on every cell.

Method	AUC	DTU		ETH3D		7-Scenes		ScanNet++		nuScenes	
		@3	@30	@3	@30	@3	@30	@3	@30	@3	@30
MASt3R [Leroy et al., 2024]	21.6	81.7	35.2	57.6	9.3	70.6	15.5	43.9	9.4	62.7	
MASt3R-SfM [Duisterhof et al., 2024]	40.2	91.4	52.8	85.0	16.4	80.3	38.7	85.0	9.1	70.9	
MapAnything [Keetha et al., 2026]	18.1	88.8	37.1	73.8	8.2	74.6	70.6	96.7	37.8	82.8	
Pi3 [Wang et al., 2025b]	70.2	97.3	43.2	84.9	11.3	81.3	76.5	97.3	24.8	82.4	
VGGT [Wang et al., 2025]	96.5	99.8	35.4	82.8	11.1	79.1	15.1	74.7	39.2	83.8	
VGGT- Ω -1B [Wang et al., 2026]	77.4	98.1	64.1	95.4	21.3	87.0	29.9	87.3	42.4	85.5	
DA3-L [Lin et al., 2025]	69.2	97.3	38.8	75.3	11.8	79.7	7.6	71.8	11.0	74.7	
DA3-G [Lin et al., 2025]	74.9	97.9	55.4	82.4	12.0	80.9	26.4	80.2	37.7	82.0	
Ours	83.2	98.8	66.0	95.4	13.9	81.7	79.4	98.0	43.4	85.3	

each use embedding dimension 384 and two transformer blocks. We sample $K \sim \text{Beta}(2, 1)$ scaled into $[8, 16]$ during training so that a single checkpoint supports any step count in this range (Table 5). We run $K_{\text{inf}} = 16$ steps at inference. We optimize with AdamW [Loshchilov and Hutter, 2019] at a base learning rate of 3×10^{-4} , weight decay 0.05, and a cosine decay schedule without warmup in the first stage, applying a $0.1 \times$ multiplier to the DINOv2 backbone. The first stage trains end-to-end for 200K iterations. The second stage finetunes the depth decoder (see Section 3.5) for 40K iterations at 1×10^{-4} with a 500-step linear warmup and a confidence regularizer weight of $\lambda_c = 0.2$. The depth, ray, pointmap, and camera losses are weighted equally, and within the camera loss, the translation, rotation, and field-of-view terms are weighted $(1, 1, 0.5)$. We apply the depth-gradient term only on synthetic data, where ground-truth depth is dense enough for reliable gradient supervision. We train on a mixture of 29 public datasets and list them in the supplemental material.

4.1 Comparison with State of the Art

Evaluation datasets. We evaluate on a set of diverse benchmarks that span indoor, outdoor, object-centric, and driving scenes: DTU [Jensen et al., 2014], ETH3D [Schöps et al., 2017], 7-Scenes [Shotton et al., 2013], ScanNet++ [Yeshwanth et al., 2023], and nuScenes [Caesar et al., 2020]. For ScanNet++, which serves as a training dataset for multiple baselines [Lin et al., 2025, Wang et al., 2025b, Keetha et al., 2026, Duisterhof et al., 2024, Leroy et al., 2024, Wang et al., 2026] and our model, we enforce a clean scene-level split between the training and evaluation data.

Evaluation metrics. We evaluate reconstruction quality with two metrics computed on the global pointmap after a Sim(3) alignment of the predicted points to the ground truth. Both are derived from the per-point relative error $r_i = \|\mathbf{X}_{\theta,i} - \mathbf{X}_{\text{gt},i}\| / \|\mathbf{X}_{\text{gt},i}\|$: the relative ℓ_2 distance (**Rel. L2** \downarrow) is its

Table 3: **Model efficiency and quality.** Parameter count, forward-pass FLOPs (total and per-image), peak inference GPU memory, and average IR / AUC@30° across the five benchmarks of Tables 1 and 2, measured on a single A100 with 24 input views. For MAST3R [Leroy et al., 2024] (swin-5, 120 pairs) and MAST3R-SfM [Duisterhof et al., 2024] (retrieval-20-10, 273 pairs), the reported FLOPs cover only the pair-network forward passes, excluding the iterative global alignment that follows. Their lower peak memory comes from processing pairs sequentially. DéjàView leads on average IR and AUC@30° at the smallest parameter count.

Method	Params (M) ↓	Compute (TFLOPs) ↓	Compute / Img (TFLOPs) ↓	Peak Mem (GiB) ↓	IR (%) ↑	AUC@30 (%) ↑
MASt3R [Leroy et al., 2024]	689	500.0	20.8	4.4	38.3	63.3
MASt3R-SfM [Duisterhof et al., 2024]	690	1150.1	47.9	3.4	60.8	82.5
MapAnything [Keetha et al., 2026]	1228	148.4	6.2	20.1	69.0	83.3
Pi3 [Wang et al., 2025b]	959	153.8	6.4	6.6	77.4	88.6
VGGT [Wang et al., 2025]	1257	190.0	7.9	14.7	66.0	84.0
VGGT-Ω-1B [Wang et al., 2026]	1144	99.8	4.2	7.9	74.8	90.7
DA3-L [Lin et al., 2025]	356	71.4	3.0	7.3	58.3	79.7
DA3-G [Lin et al., 2025]	1201	178.7	7.4	13.0	66.5	84.7
Ours	117	75.9	3.2	4.9	80.3	91.8

mean over valid points, and the inlier ratio (**IR** ↑) is the fraction of points with $r_i < 3\%$. For camera pose accuracy, we report the area under the cumulative error curve at angular thresholds of 3° and 30° (**AUC@3** ↑ and **AUC@30** ↑), where the per-pair error is the maximum of the rotation and translation angle errors.

Baselines. We compare against state-of-the-art feed-forward 3D reconstruction methods: VGGT [Wang et al., 2025], Pi3 [Wang et al., 2025b], MapAnything [Keetha et al., 2026], and Depth Anything 3 (DA3) [Lin et al., 2025]. We also include MAST3R [Leroy et al., 2024] and MAST3R-SfM [Duisterhof et al., 2024], which combine pairwise prediction with sparse global alignment. In addition, we report numbers for the concurrent work VGGT-Ω [Wang et al., 2026] for completeness. We run all baselines through our evaluation framework using their official released checkpoints, with MapAnything and DA3 at their v1.1 releases, VGGT-Ω at the 1B-512 release, and DA3 reported at two backbone scales (ViT-L and ViT-G). Per-baseline configurations are detailed in Section F.

Results. At 117M parameters and 75.9 TFLOPs of compute (Table 3), DéjàView matches or exceeds much larger feed-forward methods while running in under 5 GiB of peak memory at 24 input views. Among prior work, Pi3 [Wang et al., 2025b] is the closest competitor, leading on indoor pointmap accuracy at 8× our parameters and 2× our compute. VGGT [Wang et al., 2025] retains its lead on DTU pose at 10× our parameters, with its lead concentrated at the tightest AUC@3° threshold (96.5 vs 83.2) and shrinking to within 1.0 point at AUC@30°. The concurrent VGGT-Ω [Wang et al., 2026] edges DéjàView on outdoor pointmap Rel. L2 (ETH3D, nuScenes) and on 7-Scenes pose at 10× our parameters, but trails on every other benchmark and on the average IR and AUC@30° at the bottom of Table 3; on ScanNet++ in particular, DéjàView leads VGGT-Ω by nearly 50 points at AUC@3° and over 10 points at AUC@30°. MAST3R-SfM [Duisterhof et al., 2024] is competitive on indoor sequences but at or near the bottom of every nuScenes metric, at 15× our forward-pass cost. Overall, our method achieves top average performance across benchmarks, the highest parameter efficiency, and remains highly competitive in compute and memory cost.

4.2 Analysis

We diagnose two axes of our recurrent backbone: architectural choices in the block (Table 4), and the step count at training and inference (Table 5). All variants use a ViT-B encoder and are trained for 100K iterations on the same data, and differ only along the examined axis.

Block design. We progressively add the components of our recurrent design in Table 4, starting from a fully decoupled variant in which each of the 16 recurrent steps has its own block (no weight sharing, no time conditioning). Weight sharing collapses the 16 independent blocks into a single shared block applied recurrently. The time-conditioned residual gates (s_{attn} , s_{mlp}) modulate the block’s attention and MLP branches, and the state gate (s_{out}) yields our full method. Each component improves every

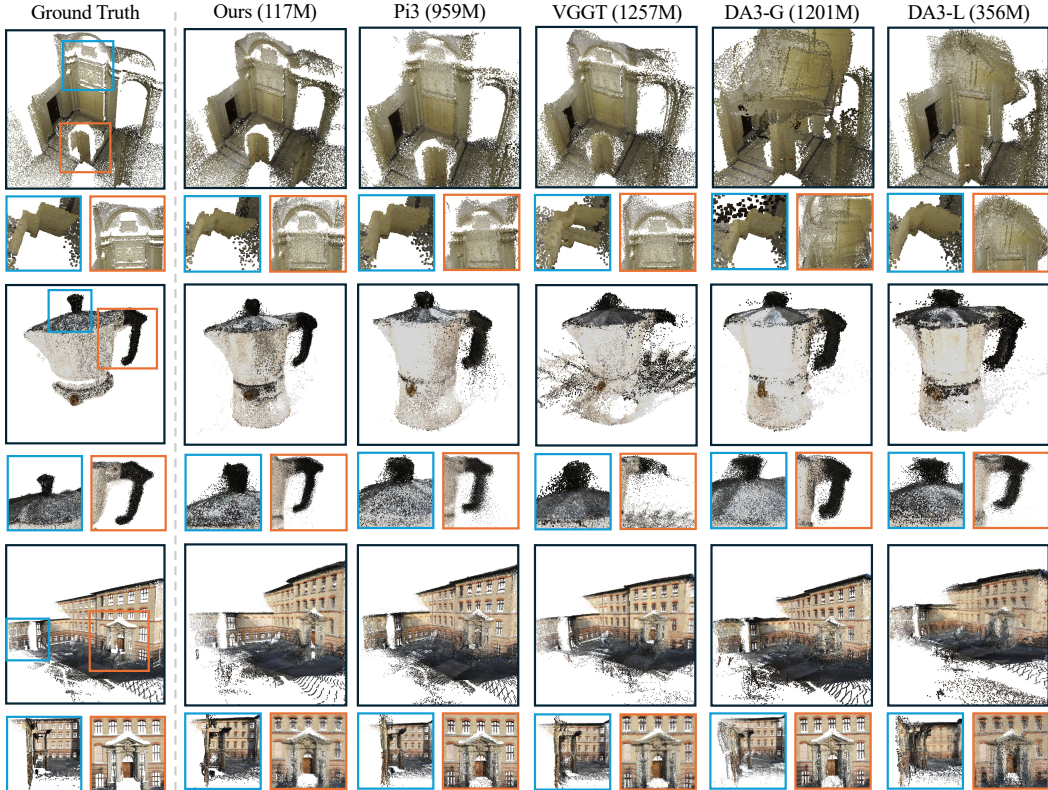


Figure 4: **Qualitative results.** Predicted point clouds for three scenes, comparing DéjàView to four feed-forward baselines with parameter counts shown above each column. DéjàView produces denser, less noisy point clouds despite using far fewer parameters.

Table 4: **Block design ablation.** We progressively add the components of our looped block. Weight sharing constrains the recurrence to a single looped block, the time-conditioned residual gates modulate the attention and MLP branches, and the state gate modulates the residual stream. We report metrics averaged across the five benchmarks of Tables 1 and 2.

Variant	Weight sharing	Residual gates ($S_{\text{attn}}, S_{\text{mlp}}$)	State gate (S_{out})	Rel. L2 ↓	IR ↑	AUC@3 ↑	AUC@30 ↑
Decoupled	✗	✗	✗	0.056	61.1	23.0	82.0
Shared	✓	✗	✗	0.045	66.4	30.2	84.8
Shared + residual gates	✓	✓	✗	0.042	67.0	31.5	85.9
Shared + state gate	✓	✓	✓	0.040	69.2	33.3	86.9

metric monotonically. Notably, weight sharing alone already outperforms the decoupled architecture despite having $16\times$ fewer parameters.

Step-count. We vary the recurrent step count at training and inference in Table 5. The fixed- K baselines train and run with a constant step count. Our variable- K model trains with $K \sim \text{Beta}(2, 1)$ on $[8, 16]$ and is evaluated at $K_{\text{inf}}=12$ and $K_{\text{inf}}=16$. At $K_{\text{inf}}=16$, variable- K training matches Fixed $K=16$ within $\sim 2\%$ on every metric. The same checkpoint, evaluated at $K_{\text{inf}}=12$, stays within $\sim 3\%$ of Fixed $K=12$ across all metrics.

5 Discussion

Modern 3D reconstruction transformers have improved primarily by scaling. We presented DéjàView, which instead applies a single shared block recurrently to a DINOv2-initialized state, sampling the step count at training so that one checkpoint covers a range of inference budgets. It matches or surpasses much larger feed-forward baselines across five reconstruction benchmarks at a fraction of

Table 5: **Step-count analysis.** Fixed- K baselines train and run with a constant step count. Our variable- K model trains with $K \sim \text{Beta}(2, 1)$ on [8, 16] and is evaluated at $K_{\text{inf}}=12$ and $K_{\text{inf}}=16$. Metrics are averaged across the five benchmarks of Tables 1 and 2. DéjàView’s variable- K training stays within $\sim 2\%$ of Fixed $K=16$ at $K_{\text{inf}}=16$ and $\sim 3\%$ of Fixed $K=12$ at $K_{\text{inf}}=12$, so a single checkpoint covers both inference budgets at near-zero quality cost.

Variant	Training K -sampler	K_{inf}	Rel. L2 ↓	IR ↑	AUC@3 ↑	AUC@30 ↑
Fixed $K=12$	fixed	12	0.044	67.6	30.4	85.5
Ours (Variable, $K_{\text{max}}=16$)	Beta on [8, 16]	12	0.043	66.7	29.6	85.4
Fixed $K=16$	fixed	16	0.041	69.6	33.8	86.8
Ours (Variable, $K_{\text{max}}=16$)	Beta on [8, 16]	16	0.040	69.2	33.3	86.9

their parameters and comparable or lower compute, suggesting that parameter scaling is not the only path forward for 3D reconstruction.

DéjàView has three main limitations. First, the trained recurrence does not extrapolate beyond its step range: a few channels diverge once K_{inf} exceeds K_{max} . Our preliminary attempts with looped-transformer stabilization [Yang et al., 2024] suggest such recipes plateau past the trained budget rather than continuing to improve, at significant additional training cost. Second, variable- K training matches rather than exceeds fixed- K at the same inference budget, trading raw quality for flexibility across budgets from one checkpoint. Finally, DéjàView does not explicitly handle dynamic scenes.

Acknowledgements

This project was partially funded by the ERC Starting Grant DynAI (ERC-101043189).

References

- Naveen Arivazhagan, Ankur Bapna, Orhan Firat, Dmitry Lepikhin, Melvin Johnson, Maxim Krikun, Mia Xu Chen, Yuan Cao, George Foster, Colin Cherry, et al. Massively multilingual neural machine translation in the wild: Findings and challenges. *arXiv preprint arXiv:1907.05019*, 2019.
- Armen Avetisyan, Christopher Xie, Henry Howard-Jenkins, Tsun-Yi Yang, Samir Aroudj, Suvam Patra, Fuyang Zhang, Duncan Frost, Luke Holland, Campbell Orme, Jakob Engel, Edward Miller, Richard Newcombe, and Vasileios Balntas. SceneScript: Reconstructing scenes with an autoregressive structured language model. In *European Conference on Computer Vision (ECCV)*, 2024.
- Shaojie Bai, J. Zico Kolter, and Vladlen Koltun. Deep equilibrium models. In *Annual Conference on Neural Information Processing Systems (NeurIPS)*, 2019.
- Arpit Bansal, Avi Schwarzschild, Eitan Borgnia, Zeyad Emam, Furong Huang, Micah Goldblum, and Tom Goldstein. End-to-end algorithm synthesis with recurrent networks: Extrapolation without overthinking. In *Annual Conference on Neural Information Processing Systems (NeurIPS)*, 2022.
- Gilad Baruch, Zhuoyuan Chen, Afshin Dehghan, Tal Dimry, Yuri Feigin, Peter Fu, Thomas Gebauer, Brandon Joffe, Daniel Kurz, Arik Schwartz, and Elad Shulman. ARKitScenes: A diverse real-world dataset for 3D indoor scene understanding using mobile RGB-D data. In *Annual Conference on Neural Information Processing Systems (NeurIPS)*, 2021.
- Michael J. Black, Priyanka Patel, Joachim Tesch, and Jinlong Yang. BEDLAM: A synthetic dataset of bodies exhibiting detailed lifelike animated motion. In *IEEE/CVF Conference on Computer Vision and Pattern Recognition (CVPR)*, 2023.
- Yohann Cabon, Naila Murray, and Martin Humenberger. Virtual KITTI 2. *arXiv preprint arXiv:2001.10773*, 2020.
- Holger Caesar, Varun Bankiti, Alex H. Lang, Sourabh Vora, Venice Erin Liong, Qiang Xu, Anush Krishnan, Yu Pan, Giancarlo Baldan, and Oscar Beijbom. nuScenes: A multimodal dataset for autonomous driving. In *IEEE/CVF Conference on Computer Vision and Pattern Recognition (CVPR)*, 2020.

- Aleksander Colovic, Arno Knapitsch, Lorenzo Porzi, and Samuel Rota Bulò. Mapillary metropolis dataset. <https://www.mapillary.com/dataset/metropolis>, 2021.
- Angela Dai, Angel X. Chang, Manolis Savva, Maciej Halber, Thomas Funkhouser, and Matthias Nießner. ScanNet: Richly-annotated 3D reconstructions of indoor scenes. In *IEEE/CVF Conference on Computer Vision and Pattern Recognition (CVPR)*, 2017.
- Timothée Darcet, Maxime Oquab, Julien Mairal, and Piotr Bojanowski. Vision transformers need registers. In *International Conference on Learning Representations (ICLR)*, 2024.
- Mostafa Dehghani, Stephan Gouws, Oriol Vinyals, Jakob Uszkoreit, and Lukasz Kaiser. Universal transformers. In *International Conference on Learning Representations (ICLR)*, 2019.
- Matt Deitke, Dustin Schwenk, Jordi Salvador, Luca Weihs, Oscar Michel, Eli VanderBilt, Ludwig Schmidt, Kiana Ehsani, Aniruddha Kembhavi, and Ali Farhadi. Objaverse: A universe of annotated 3D objects. In *IEEE/CVF Conference on Computer Vision and Pattern Recognition (CVPR)*, 2023.
- Alexey Dosovitskiy, Lucas Beyer, Alexander Kolesnikov, Dirk Weissenborn, Xiaohua Zhai, Thomas Unterthiner, Mostafa Dehghani, Matthias Minderer, Georg Heigold, Sylvain Gelly, Jakob Uszkoreit, and Neil Houlsby. An image is worth 16x16 words: Transformers for image recognition at scale. In *International Conference on Learning Representations (ICLR)*, 2021.
- Bardienus Duisterhof, Lojze Zust, Philippe Weinzaepfel, Vincent Leroy, Yohann Cabon, and Jerome Revaud. MAST3R-SfM: a fully-integrated solution for unconstrained structure-from-motion. *arXiv preprint arXiv:2409.19152*, 2024.
- Sven Elfle, Ruilong Li, Sérgio Agostinho, Zan Gojcic, Laura Leal-Taixé, Qunjie Zhou, and Aljosa Osep. Vgg-t³: Offline feed-forward 3d reconstruction at scale. In *Proceedings of the IEEE/CVF Conference on Computer Vision and Pattern Recognition (CVPR)*, 2026.
- Xianze Fang, Jingnan Gao, Zhe Wang, Zhuo Chen, Xingyu Ren, Jiangjing Lyu, Qiaomu Ren, Zhonglei Yang, Xiaokang Yang, Yichao Yan, and Chengfei Lyu. Dens3r: A foundation model for 3d geometry prediction. In *The Fourteenth International Conference on Learning Representations*, 2026.
- Michaël Fonder and Marc Van Droogenbroeck. Mid-Air: A multi-modal dataset for extremely low altitude drone flights. In *IEEE/CVF Conference on Computer Vision and Pattern Recognition (CVPR) Workshops*, 2019.
- Jonas Geiping, Sean Michael McLeish, Neel Jain, John Kirchenbauer, Siddharth Singh, Brian R. Bartoldson, Bhavya Kailkhura, Abhinav Bhatnagar, and Tom Goldstein. Scaling up test-time compute with latent reasoning: A recurrent depth approach. In *Annual Conference on Neural Information Processing Systems (NeurIPS)*, 2025.
- Alex Graves. Adaptive computation time for recurrent neural networks, 2017.
- Klaus Greff, Francois Belletti, Lucas Beyer, Carl Doersch, Yilun Du, Daniel Duckworth, David J. Fleet, Dan Gnanapragasam, Florian Golemo, Charles Herrmann, Thomas Kipf, Abhijit Kundu, Dmitry Lagun, Issam Laradji, Hsueh-Ti Derek Liu, Henning Meyer, Yishu Miao, Derek Nowrouzezahrai, Cengiz Oztireli, Etienne Pot, Noha Radwan, Daniel Rebain, Sara Sabour, Mehdi S. M. Sajjadi, Matan Sela, Vincent Sitzmann, Austin Stone, Deqing Sun, Suhani Vora, Ziyu Wang, Tianhao Wu, Kwang Moo Yi, Fangcheng Zhong, and Andrea Tagliasacchi. Kubric: A scalable dataset generator. In *IEEE/CVF Conference on Computer Vision and Pattern Recognition (CVPR)*, 2022.
- Byeongho Heo, Song Park, Dongyoon Han, and Sangdoon Yun. Rotary position embedding for vision transformer. In *European Conference on Computer Vision (ECCV)*, 2024.
- Junjie Hu, Mete Ozay, Yan Zhang, and Takayuki Okatani. Revisiting single image depth estimation: Toward higher resolution maps with accurate object boundaries. 2019.
- Jiahui Huang, Qunjie Zhou, Hesam Rabeti, Aleksandr Korovko, Huan Ling, Xuanchi Ren, Tianchang Shen, Jun Gao, Dmitry Slepichev, Chen-Hsuan Lin, et al. Vipe: Video pose engine for 3d geometric perception. *arXiv preprint arXiv:2508.10934*, 2025.

- Po-Han Huang, Kevin Matzen, Johannes Kopf, Narendra Ahuja, and Jia-Bin Huang. DeepMVS: Learning multi-view stereopsis. In *IEEE/CVF Conference on Computer Vision and Pattern Recognition (CVPR)*, 2018.
- DeLesley Hutchins, Imanol Schlag, Yuhuai Wu, Ethan Dyer, and Behnam Neyshabur. Block-recurrent transformers. In Alice H. Oh, Alekh Agarwal, Danielle Belgrave, and Kyunghyun Cho, editors, *Annual Conference on Neural Information Processing Systems (NeurIPS)*, 2022.
- Mozes Jacobs, Thomas Fel, Richard Hakim, Alessandra Brondetta, Demba E. Ba, and T. Anderson Keller. Block recurrent dynamics in vision transformers. In *International Conference on Learning Representations (ICLR)*, 2026.
- Rasmus Jensen, Anders Dahl, George Vogiatzis, Engin Tola, and Henrik Aanæs. Large scale multi-view stereopsis evaluation. In *IEEE/CVF Conference on Computer Vision and Pattern Recognition (CVPR)*, 2014.
- Gyeongjin Kang, Seungtae Nam, Xiangyu Sun, Sameh Khamis, Abdelrahman Mohamed, and Eunbyung Park. ilrm: An iterative large 3d reconstruction model. In *IEEE/CVF Conference on Computer Vision and Pattern Recognition (CVPR)*, 2026.
- Nikita Karaev, Ignacio Rocco, Benjamin Graham, Natalia Neverova, Andrea Vedaldi, and Christian Rupprecht. DynamicStereo: Consistent dynamic depth from stereo videos. In *IEEE/CVF Conference on Computer Vision and Pattern Recognition (CVPR)*, 2023.
- Nikhil Keetha, Norman Müller, Johannes Schönberger, Lorenzo Porzi, Yuchen Zhang, Tobias Fischer, Arno Knapitsch, Duncan Zauss, Ethan Weber, Nelson Antunes, Jonathon Luiten, Manuel Lopez-Antequera, Samuel Rota Bulò, Christian Richardt, Deva Ramanan, Sebastian Scherer, and Peter Kotschieder. MapAnything: Universal feed-forward metric 3D reconstruction. In *International Conference on 3D Vision (3DV)*, 2026.
- Alexander Kirillov, Eric Mintun, Nikhila Ravi, Hanzi Mao, Chloé Rolland, Laura Gustafson, Tete Xiao, Spencer Whitehead, Alexander C. Berg, Wan-Yen Lo, Piotr Dollár, and Ross Girshick. Segment anything. In *International Conference on Computer Vision (ICCV)*, 2023.
- Zhenzhong Lan, Mingda Chen, Sebastian Goodman, Kevin Gimpel, Piyush Sharma, and Radu Soricut. Albert: A lite bert for self-supervised learning of language representations. In *International Conference on Learning Representations (ICLR)*, 2020.
- Justin Lazarow, David Griffiths, Gefen Kohavi, Francisco Crespo, and Afshin Dehghan. Cubify anything: Scaling indoor 3D object detection. In *IEEE/CVF Conference on Computer Vision and Pattern Recognition (CVPR)*, 2025.
- Vincent Leroy, Yann Cabon, and Jérôme Revaud. Grounding image matching in 3D with MAST3R. In *European Conference on Computer Vision (ECCV)*, 2024.
- Yixuan Li, Lihan Jiang, Linning Xu, Yuanbo Xiangli, Zhenzhi Wang, Dahua Lin, and Bo Dai. MatrixCity: A large-scale city dataset for city-scale neural rendering and beyond. In *International Conference on Computer Vision (ICCV)*, 2023.
- Zhengqi Li and Noah Snavely. MegaDepth: Learning single-view depth prediction from internet photos. In *IEEE/CVF Conference on Computer Vision and Pattern Recognition (CVPR)*, 2018.
- Haotong Lin, Sili Chen, Junhao Liew, Donny Y Chen, Zhenyu Li, Guang Shi, Jiashi Feng, and Bingyi Kang. Depth anything 3: Recovering the visual space from any views. *arXiv preprint arXiv:2511.10647*, 2025.
- Lu Ling, Yichen Sheng, Zhi Tu, Wentian Zhao, Cheng Xin, Kun Wan, Lantao Yu, Qianyu Guo, Zixun Yu, Yawen Lu, Xuanmao Li, Xingpeng Sun, Rohan Ashok, Aniruddha Mukherjee, Hao Kang, Xiangrui Kong, Gang Hua, Tianyi Zhang, Bedrich Benes, and Aniket Bera. DL3DV-10K: A large-scale scene dataset for deep learning-based 3D vision. In *IEEE/CVF Conference on Computer Vision and Pattern Recognition (CVPR)*, 2024.
- Lahav Lipson, Zachary Teed, and Jia Deng. Raft-stereo: Multilevel recurrent field transforms for stereo matching. In *International Conference on 3D Vision (3DV)*, 2021.

- Manuel López-Antequera, Pau Gargallo, Markus Hofinger, Samuel Rota Bulò, Yubin Kuang, and Peter Kotschieder. Mapillary planet-scale depth dataset. In *European Conference on Computer Vision (ECCV)*, 2020.
- Ilya Loshchilov and Frank Hutter. Decoupled weight decay regularization. In *International Conference on Learning Representations (ICLR)*, 2019.
- Yihang Luo, Shangchen Zhou, Yushi Lan, Xingang Pan, and Chen Change Loy. 4rc: 4d reconstruction via conditional querying anytime and anywhere. In *ICML*, 2026.
- Lukas Mehl, Jenny Schmalfluss, Azin Jahedi, Yaroslava Nalivayko, and Andrés Bruhn. Spring: A high-resolution high-detail dataset and benchmark for scene flow, optical flow and stereo. In *IEEE/CVF Conference on Computer Vision and Pattern Recognition (CVPR)*, 2023.
- Maxime Oquab, Timothée Darcet, Théo Moutakanni, Huy Vo, Marc Szafraniec, Vasil Khalidov, Pierre Fernandez, Daniel Haziza, Francisco Massa, Alaaeldin El-Nouby, et al. DINOv2: Learning robust visual features without supervision. *Transactions on Machine Learning Research (TMLR)*, 2024.
- Linfei Pan, Dániel Baráth, Marc Pollefeys, and Johannes L Schönberger. Global structure-from-motion revisited. In *European Conference on Computer Vision (ECCV)*, 2024.
- Adam Paszke, Sam Gross, Francisco Massa, Adam Lerer, James Bradbury, Gregory Chanan, Trevor Killeen, Zeming Lin, Natalia Gimelshein, Luca Antiga, et al. Pytorch: An imperative style, high-performance deep learning library. 2019.
- Alec Radford, Jong Wook Kim, Chris Hallacy, Aditya Ramesh, Gabriel Goh, Sandhini Agarwal, Girish Sastry, Amanda Askell, Pamela Mishkin, Jack Clark, Gretchen Krueger, and Ilya Sutskever. Learning transferable visual models from natural language supervision. In *International Conference on Machine Learning (ICML)*, 2021.
- Jeremy Reizenstein, Roman Shapovalov, Philipp Henzler, Luca Sbordone, Patrick Labatut, and David Novotny. Common objects in 3D: Large-scale learning and evaluation of real-life 3D category reconstruction. In *International Conference on Computer Vision (ICCV)*, 2021.
- Mike Roberts, Jason Ramapuram, Anurag Ranjan, Atulit Kumar, Miguel Angel Bautista, Nathan Paczan, Russ Webb, and Joshua M. Susskind. Hypersim: A photorealistic synthetic dataset for holistic indoor scene understanding. In *International Conference on Computer Vision (ICCV)*, 2021.
- Nikunj Saunshi, Nishanth Dikkala, Zhiyuan Li, Sanjiv Kumar, and Sashank J. Reddi. Reasoning with latent thoughts: On the power of looped transformers. In *International Conference on Learning Representations (ICLR)*, 2025.
- Johannes Lutz Schönberger and Jan-Michael Frahm. Structure-from-motion revisited. In *IEEE/CVF Conference on Computer Vision and Pattern Recognition (CVPR)*, 2016.
- Thomas Schöps, Johannes Lutz Schönberger, Silvano Galliani, Torsten Sattler, Konrad Schindler, Marc Pollefeys, and Andreas Geiger. A multi-view stereo benchmark with high-resolution images and multi-camera videos. In *IEEE/CVF Conference on Computer Vision and Pattern Recognition (CVPR)*, 2017.
- Avi Schwarzschild, Eitan Borgnia, Arjun Gupta, Furong Huang, Uzi Vishkin, Micah Goldblum, and Tom Goldstein. Can you learn an algorithm? generalizing from easy to hard problems with recurrent networks. In *Annual Conference on Neural Information Processing Systems (NeurIPS)*, 2021.
- Jamie Shotton, Ben Glocker, Christopher Zach, Shahram Izadi, Antonio Criminisi, and Andrew Fitzgibbon. Scene coordinate regression forests for camera relocalization in RGB-D images. In *IEEE/CVF Conference on Computer Vision and Pattern Recognition (CVPR)*, 2013.
- Michal Starý, Julien Gaubil, Ayush Tewari, and Vincent Sitzmann. Understanding Multi-View Transformers. In *ICCV 2025 E2E3D Workshop*, 2025.

- Julian Straub, Thomas Whelan, Lingni Ma, Yufan Chen, Erik Wijmans, Simon Green, Jakob J. Engel, Raul Mur-Artal, Carl Ren, Shobhit Verma, Anton Clarkson, Mingfei Yan, Brian Budge, Yajie Yan, Xiaqing Pan, June Yon, Yuyang Zou, Kimberly Leon, Nigel Carter, Jesus Briales, Tyler Gillingham, Elias Mueggler, Luis Pesqueira, Manolis Savva, Dhruv Batra, Hauke M. Strasdat, Renzo De Nardi, Michael Goesele, Steven Lovegrove, and Richard Newcombe. The replica dataset: A digital replica of indoor spaces. *arXiv preprint arXiv:1906.05797*, 2019.
- Edgar Sucar, Eldar Insafutdinov, Zihang Lai, and Andrea Vedaldi. V-DPM: 4d video reconstruction with dynamic point maps. In *Proceedings of the IEEE/CVF Conference on Computer Vision and Pattern Recognition (CVPR)*, 2026.
- Pei Sun, Henrik Kretzschmar, Xerxes Dotiwalla, Aurelien Chouard, Vijaysai Patnaik, Paul Tsui, James Guo, Yin Zhou, Yuning Chai, Benjamin Caine, Vijay Vasudevan, Wei Han, Jiquan Ngiam, Hang Zhao, Aleksei Timofeev, Scott Ettinger, Maxim Krivokon, Amy Gao, Aditya Joshi, Yu Zhang, Jonathon Shlens, Zhifeng Chen, and Dragomir Anguelov. Scalability in perception for autonomous driving: Waymo open dataset. In *IEEE/CVF Conference on Computer Vision and Pattern Recognition (CVPR)*, 2020.
- Zachary Teed and Jia Deng. RAFT: Recurrent all-pairs field transforms for optical flow. In *European Conference on Computer Vision (ECCV)*, 2020.
- Zachary Teed and Jia Deng. DROID-SLAM: Deep visual SLAM for monocular, stereo, and RGB-D cameras. In *Annual Conference on Neural Information Processing Systems (NeurIPS)*, 2021.
- Fabio Tosi, Yiyi Liao, Carolin Schmitt, and Andreas Geiger. SMD-Nets: Stereo mixture density networks. In *IEEE/CVF Conference on Computer Vision and Pattern Recognition (CVPR)*, 2021.
- Hugo Touvron, Matthieu Cord, Alexandre Sablayrolles, Gabriel Synnaeve, and Hervé Jégou. Going deeper with image transformers. In *International Conference on Computer Vision (ICCV)*, 2021.
- Basile Van Hoorick, Rundi Wu, Ege Ozguroglu, Kyle Sargent, Ruoshi Liu, Pavel Tokmakov, Achal Dave, Changxi Zheng, and Carl Vondrick. Generative camera dolly: Extreme monocular dynamic novel view synthesis. In *European Conference on Computer Vision (ECCV)*, 2024.
- Fangjinhua Wang, Silvano Galliani, Christoph Vogel, and Marc Pollefeys. Itermvs: Iterative probability estimation for efficient multi-view stereo. In *IEEE/CVF Conference on Computer Vision and Pattern Recognition (CVPR)*, 2022.
- Hengyi Wang and Lourdes Agapito. 3d reconstruction with spatial memory. In *International Conference on 3D Vision (3DV)*, 2025.
- Jianyuan Wang, Minghao Chen, Nikita Karaev, Andrea Vedaldi, Christian Rupprecht, and David Novotny. VGGT: Visual geometry grounded transformer. In *IEEE/CVF Conference on Computer Vision and Pattern Recognition (CVPR)*, 2025.
- Jianyuan Wang, Minghao Chen, Shangzhan Zhang, Nikita Karaev, Johannes Schönberger, Patrick Labatut, Piotr Bojanowski, David Novotny, Andrea Vedaldi, and Christian Rupprecht. VGGT- Ω . In *Proceedings of the IEEE/CVF Conference on Computer Vision and Pattern Recognition (CVPR)*, 2026.
- Kaixuan Wang and Shaojie Shen. Flow-motion and depth network for monocular stereo and beyond. *IEEE Robotics and Automation Letters (RAL)*, 5(2):3307–3314, 2020.
- Qianqian Wang*, Yifei Zhang*, Aleksander Holynski, Alexei A. Efros, and Angjoo Kanazawa. Continuous 3d perception model with persistent state. In *IEEE/CVF Conference on Computer Vision and Pattern Recognition (CVPR)*, 2025.
- Ruicheng Wang, Sicheng Xu, Cassie Dai, Jianfeng Xiang, Yu Deng, Xin Tong, and Jiaolong Yang. Moge: Unlocking accurate monocular geometry estimation for open-domain images with optimal training supervision. In *Proceedings of the IEEE/CVF Conference on Computer Vision and Pattern Recognition*, pages 5261–5271, 2025a.

- Shuzhe Wang, Vincent Leroy, Yohann Cabon, Boris Chidlovskii, and Jérôme Revaud. DUS_t3R: Geometric 3D vision made easy. In *IEEE/CVF Conference on Computer Vision and Pattern Recognition (CVPR)*, 2024.
- Wenshan Wang, DeLong Zhu, Xiangwei Wang, Yaoyu Hu, Yuheng Qiu, Chen Wang, Yafei Hu, Ashish Kapoor, and Sebastian Scherer. TartanAir: A dataset to push the limits of visual SLAM. In *IEEE/RSJ International Conference on Intelligent Robots and Systems (IROS)*, 2020.
- Yifan Wang, Jianjun Zhou, Haoyi Zhu, Wenzheng Chang, Yang Zhou, Zizun Li, Junyi Chen, Jiangmiao Pang, Chunhua Shen, and Tong He. π^3 : Permutation-equivariant visual geometry learning. *arXiv preprint arXiv:2507.13347*, 2025b.
- Philippe Weinzaepfel, Vincent Leroy, Thomas Lucas, Romain Brégier, Yohann Cabon, Vaibhav Arora, Leonid Antsfeld, Boris Chidlovskii, Gabriela Csurka, and Jerome Revaud. Croco: Self-supervised pre-training for 3d vision tasks by cross-view completion. In *Annual Conference on Neural Information Processing Systems (NeurIPS)*, 2022.
- Yuxin Wen, John Kirchenbauer, Jonas Geiping, and Tom Goldstein. Tree-ring watermarks: Fingerprints for diffusion images that are invisible and robust. In *Annual Conference on Neural Information Processing Systems (NeurIPS)*, 2023.
- Hongchi Xia, Yang Fu, Sifei Liu, and Xiaolong Wang. RGBD objects in the wild: Scaling real-world 3D object learning from RGB-D videos. In *IEEE/CVF Conference on Computer Vision and Pattern Recognition (CVPR)*, 2024.
- Jianfeng Xiang, Zelong Lv, Sicheng Xu, Yu Deng, Ruicheng Wang, Bowen Zhang, Dong Chen, Xin Tong, and Jiaolong Yang. Structured 3D latents for scalable and versatile 3D generation. In *IEEE/CVF Conference on Computer Vision and Pattern Recognition (CVPR)*, 2025.
- Jianing Yang, Alexander Sax, Kevin J. Liang, Mikael Henaff, Hao Tang, Ang Cao, Joyce Chai, Franziska Meier, and Matt Feiszli. Fast3r: Towards 3d reconstruction of 1000+ images in one forward pass. In *IEEE/CVF Conference on Computer Vision and Pattern Recognition (CVPR)*, 2025.
- Liu Yang, Kangwook Lee, Robert D Nowak, and Dimitris Papailiopoulos. Looped transformers are better at learning learning algorithms. In *International Conference on Learning Representations (ICLR)*, 2024.
- Yao Yao, Zixin Luo, Shiwei Li, Tian Fang, and Long Quan. Mvsnet: Depth inference for unstructured multi-view stereo. 2018.
- Yao Yao, Zixin Luo, Shiwei Li, Jingyang Zhang, Yufan Ren, Lei Zhou, Tian Fang, and Long Quan. BlendedMVS: A large-scale dataset for generalized multi-view stereo networks. In *IEEE/CVF Conference on Computer Vision and Pattern Recognition (CVPR)*, 2020.
- Botao Ye, Sifei Liu, Haofei Xu, Li Xueting, Marc Pollefeys, Ming-Hsuan Yang, and Peng Songyou. No pose, no problem: Surprisingly simple 3d gaussian splats from sparse unposed images. In *International Conference on Learning Representations (ICLR)*, 2025.
- Chandan Yeshwanth, Yueh-Cheng Liu, Matthias Nießner, and Angela Dai. ScanNet++: A high-fidelity dataset of 3D indoor scenes. In *International Conference on Computer Vision (ICCV)*, 2023.
- Amir R. Zamir, Alexander Sax, William Shen, Leonidas Guibas, Jitendra Malik, and Silvio Savarese. Taskonomy: Disentangling task transfer learning. In *IEEE/CVF Conference on Computer Vision and Pattern Recognition (CVPR)*, 2018.
- Xiaohua Zhai, Alexander Kolesnikov, Neil Houlsby, and Lucas Beyer. Scaling vision transformers. In *IEEE/CVF Conference on Computer Vision and Pattern Recognition (CVPR)*, 2022.
- Junyi Zhang, Charles Herrmann, Junhwa Hur, Varun Jampani, Trevor Darrell, Forrester Cole, Deqing Sun, and Ming-Hsuan Yang. Monst3r: A simple approach for estimating geometry in the presence of motion. In *International Conference on Learning Representations (ICLR)*, 2025.

Supplementary Material for Déjà View

A Training Datasets

We train on a mixture of 29 publicly available datasets that span synthetic renderings, indoor and outdoor real captures, multi-view object scans, and driving footage. The corpus is highly imbalanced: per-dataset image counts N_i span more than three orders of magnitude (from ~ 10 k for Spring to ~ 11.8 M for Aria Synthetic Environments), so naive proportional sampling would let a handful of large datasets dominate training, while uniform sampling would massively oversample the smallest ones. In LLM literature, multilingual training faces the same imbalance across high- and low-resource languages, which is addressed with temperature sampling [Arivazhagan et al., 2019]. We adopt the same recipe, treating each dataset as a “language” with token budget N_i : the probability of drawing a training example from dataset i is set to

$$p_i = \frac{N_i^\alpha}{\sum_j N_j^\alpha}, \quad \alpha = 0.5,$$

i.e. proportional to $\sqrt{N_i}$, which flattens the head of the distribution while still favouring the larger, more diverse corpora. The realised epoch share for each dataset is reported in Table 6.

B Two-Stage Depth Training

The linear pixel-shuffle head maps patch tokens to per-pixel depth via pixel shuffling. For ray directions, this is acceptable as patch-border gradients are within $\sim 10\%$ of intra-patch values. For depth, the same gradients are roughly an order of magnitude larger, producing visible block artifacts at patch boundaries (Figure 5).

We address this with two-stage training (Section 3.5). The first stage trains the model end-to-end with a linear pixel-shuffle depth head and plain ℓ_2 depth loss. Training the final pipeline configuration (convolutional head with confidence loss) end-to-end instead yields worse metrics across our benchmarks (Table 7). The second stage swaps it in, freezes the rest of the network, and finetunes the depth decoder with a confidence-weighted loss. Its convolutions smooth across patch boundaries, eliminating the block pattern (Figure 5) and yielding a slight improvement in Inlier Ratio (Table 8). As a result, we also obtain a depth confidence channel that can be used downstream to filter regions with uncertain reconstruction.

C Emergent Iterative Correspondence Search

We probe the global attention sub-block of our recurrent layer to investigate how its attention pattern evolves across iterations. For a query patch in view 0, at each iteration t we read the per-head queries and keys $Q_h^{(t)}, K_h^{(t)}$ post q - k -LayerNorm and visualize the head-averaged scaled-dot-product attention weights

$$\bar{a}^{(t)} = \frac{1}{H} \sum_{h=1}^H \text{softmax}\left(q_h^{(t)} K_h^{(t)\top} / \sqrt{d_h}\right),$$

sliced to the patch tokens of each target view and shown as a $H_p \times W_p$ heatmap. Figure 6 illustrates that the attention starts diffuse and progressively concentrates on the corresponding counterpart of the queried patch, correctly resolving symmetries and attending to all geometrically equivalent patches. This suggests that the recurrent loop implements an emergent iterative correspondence search, despite the model being supervised only on 3D reconstruction and pose estimation losses.

D Scaling Beyond K_{\max}

DéjàView is trained with an iteration count sampled per-batch as $K \sim \text{Beta}(2, 1)$ scaled to $[K_{\min}, K_{\max}]$ with $K_{\max} = 16$. We sweep K_{\min} at test time beyond K_{\max} and observe that Pose AUC@3° peaks near the trained budget, then starts to degrade after. Pose AUC@30° and

Table 6: Per-epoch training-mixture share for the 29 datasets, sorted by share. By construction, mix % = $p_i \propto \sqrt{N_i}$ where N_i is the total number of training images in dataset i .

Dataset	mix %	Dataset	mix %
Aria Synth. Env. [Avetisyan et al., 2024]	13.77	BEDLAM [Black et al., 2023]	1.99
WildRGB-D [Xia et al., 2024]	9.32	BlendedMVS [Yao et al., 2020]	1.35
TRELLIS [Xiang et al., 2025, Deitke et al., 2023]	9.04	MegaDepth [Li and Snavely, 2018]	1.16
CO3D [Reizenstein et al., 2021]	8.84	Replica [Straub et al., 2019]	0.95
Taskonomy [Zamir et al., 2018]	7.26	Virtual KITTI 2 [Cabon et al., 2020]	0.83
ScanNet [Dai et al., 2017]	6.23	Hypersim [Roberts et al., 2021]	0.69
DL3DV [Ling et al., 2024]	5.84	Kubric [Greff et al., 2022]	0.60
Cubify Any. [Lazarow et al., 2025, Baruch et al., 2021]	5.73	GTA-SfM [Wang and Shen, 2020]	0.52
TartanAir V2 [Wang et al., 2020]	4.78	MatrixCity [Li et al., 2023]	0.49
Parallel Dom. 4D [Van Hoorick et al., 2024]	4.75	MPSD [López-Antequera et al., 2020]	0.49
ScanNet++ [Yeshwanth et al., 2023]	3.96	Mapillary Metr. [Colovic et al., 2021]	0.47
Waymo [Sun et al., 2020]	2.76	UnrealStereo4K [Tosi et al., 2021]	0.44
Mid-Air [Fonder and Van Droogenbroeck, 2019]	2.61	MVS-Synth [Huang et al., 2018]	0.44
Dynamic Replica [Karaev et al., 2023]	2.16	Spring [Mehl et al., 2023]	0.40
TartanAir [Wang et al., 2020]	2.13		

Table 7: **End-to-end vs. two-stage training.** Training the final pipeline configuration end-to-end (top, convolutional head with confidence loss) consistently underperforms the first stage of our recipe (bottom, linear head with ℓ_2 depth loss) on every metric.

Variant	AUC@3° ↑	AUC@30° ↑	IR ↑	AbsRel ↓
Convolutional head + confidence loss (end-to-end)	23.0	77.1	56.5	0.152
Linear head + ℓ_2 (our stage 1)	31.0	80.6	59.2	0.125

Pointmap Rel. L2 remain stable up to approximately $K_{\text{inf}} = 30$ but eventually collapse. Figure 7 shows that model iterations cannot be pushed arbitrarily far.

Our analysis shows that this occurs because some feature channels grow unbounded as we scale beyond K_{max} . The mechanism is already visible inside the trained range (Figure 3b): while cosine similarity to $\mathbf{z}_{K_{\text{max}}}$ saturates near 1 and the relative feature update decays, the state norm $\|\mathbf{z}_k\|_2$ keeps growing monotonically through K_{max} after a short initial contraction. Iterating beyond K_{max} simply extrapolates this persistent drift: a handful of channels grow without bounds, producing the observed collapse.

E Scaling Below K_{max}

A sub- K_{max} compute allows two strategies: a full K_{inf} -step forward with uniform time interval conditioning calibrated for that budget, or early-stopping a K_{max} -step rollout by reading \mathbf{z}_k at $k = K_{\text{inf}}$. Figure 8 shows the full pass strictly dominates early-stopping for every $k < K_{\text{max}}$, with the largest gap at the smallest budget. At $K_{\text{inf}} = 8$, Pose AUC@3° rises from 0.31 to 0.44 (~43% relative improvement).

F Baseline Configurations

We run all baselines through our evaluation framework using their official code releases and checkpoints, and apply the same Sim(3) alignment to predicted pointmaps before computing metrics (Section 4.1). For Rel. L2 and IR we use each method’s primary 3D output: depth-unprojected pointmaps for VGGT, DA3, and our model, the direct point-head output for Pi3 and MapAnything, and the SGA-optimized dense pointmap for MAST3R and MAST3R-SfM.

VGGT [Wang et al., 2025]. The official facebook/VGGT-1B checkpoint at 518-pixel longest edge with patch size 14.

Table 8: **Stage 2 finetuning.** Finetuning our stage 1 model (linear head + ℓ_2 depth loss) with the convolutional head and confidence-weighted loss (stage 2) yields a small, consistent gain in Inlier Ratio while leaving the pose metrics unchanged.

Variant	AUC@3° \uparrow	AUC@30° \uparrow	IR \uparrow	AbsRel \downarrow
Linear head + ℓ_2 (stage 1, full recipe)	56.8	91.8	79.8	0.031
Conv. head + conf. loss (stage 2 finetune)	56.8	91.8	80.3	0.031

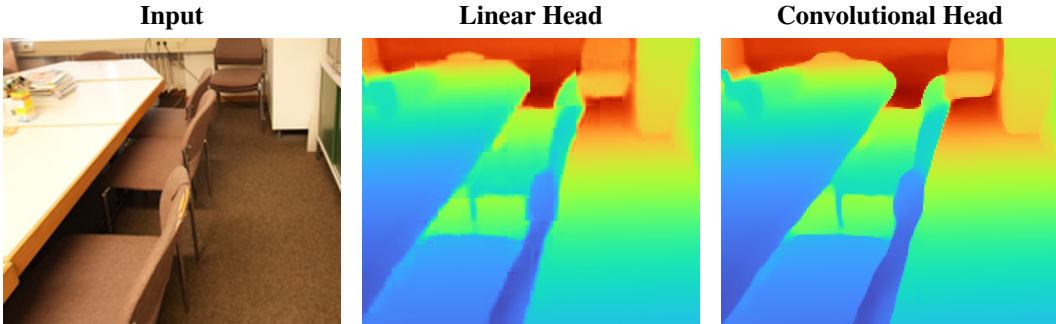


Figure 5: **Block artifacts.** Depth predicted by the first-stage linear head (**center**) shows visible block artifacts aligned with the DINOv2 patch grid. The second-stage finetune with the convolutional head (**right**) eliminates them and improves Inlier Ratio.

VGGT- Ω [Wang et al., 2026]. The official facebook/VGGT-Omega 1B checkpoint (vggt_omega_1b_512.pt, without text alignment) at 512-pixel longest edge with patch size 16. We decode the released 9D camera encoding (translation, quaternion, FoV_h , FoV_w) via the official encoding_to_camera utility and use depth-unprojected pointmaps as the primary 3D output, matching the convention used for VGGT and DA3.

Pi3 [Wang et al., 2025b]. The official yyfz233/Pi3 checkpoint at 518-pixel longest edge with patch size 14.

MapAnything [Keetha et al., 2026]. The official facebook/map-anything v1.1 checkpoint at 518-pixel longest edge with patch size 14.

Depth Anything 3 (DA3) [Lin et al., 2025]. The official v1.1 checkpoints at two backbone scales (DA3-L: depth-anything/DA3-LARGE, ViT-L, 356M params; DA3-G: depth-anything/DA3-GIANT, ViT-G, 1.2B params), both at 504-pixel longest edge with patch size 14. We decode camera pose from predicted rays.

MASt3R [Leroy et al., 2024]. The official MAST3R_ViTLarge_BaseDecoder_512_catmlpdpt_metric (metric-scale) checkpoint at 512-pixel longest edge with patch size 16, using DUST3R-style image normalization (mean and std 0.5). Pair selection is adaptive on scene size: complete (all pairs) for scenes with $N \leq 8$ views, and swin-5 (sliding window of 5) otherwise. The efficiency measurement at $N=24$ uses the swin-5 branch (120 pairs). The sparse global alignment uses the published defaults: 300 iterations of coarse alignment at learning rate 0.07 followed by 300 iterations of refinement at 0.01, with per-pixel depth optimization enabled (optim_level=refine+depth) and matching-confidence threshold 5.0. Camera intrinsics are shared across views for the single-camera benchmarks (7-Scenes, ScanNet++, nuScenes, DTU) and estimated per-view otherwise (ETH3D).

MASt3R-SfM [Duisterhof et al., 2024]. The same MAST3R checkpoint paired with the official training-free retrieval model (MASt3R_ViTLarge_BaseDecoder_512_catmlpdpt_metric_retrieval_trainingfree). Scene graphs are built via top-20 retrieval anchors with top-10 retrieved neighbors per anchor



Figure 6: **Emergent iterative correspondence search.** For two example query patches (green square) we visualize the head-averaged global self-attention sub-block weights induced by that query at each iteration of the loop, overlaid on the corresponding target view. Iterations advance left-to-right, the attention starts diffuse and progressively concentrates on the corresponding counterpart of the queried patch, despite the absence of any explicit feature matching supervision during training.

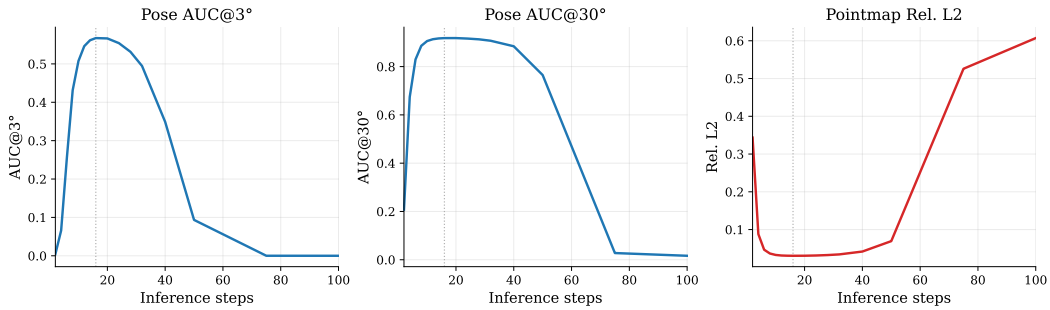


Figure 7: **Step-count extrapolation.** Test-time metrics as a function of the inference step count K_{inf} . Performance peaks at the maximum trained budget, then degrades when moving far outside the trained range.

(retrieval-20-10), yielding 273 pairs at $N=24$. The sparse global alignment uses the same hyperparameters as MAST3R, including the same per-dataset shared-intrinsics policy.

G Societal Impact

DéjàView reconstructs 3D geometry and camera poses from images. While this capability is not new, our work brings strong reconstruction quality within reach at a smaller scale than recent feed-forward baselines, lowering the overall cost of deployment. Because the model outputs geometry rather than photorealistic imagery, the direct risk of deceptive media generation is lower than for image or video synthesis models, though deployments that combine reconstruction with generative rendering should still consider provenance signals such as watermarking [Wen et al., 2023]. From an environmental perspective, our ViT-B model is trained on 128 H100 GPUs, comparable to other recent feed-forward reconstruction methods. At inference, however, it operates with roughly an order of magnitude fewer parameters and a memory footprint of under 5 GiB at 24 input views, reducing the per-query resource cost of deployment relative to the larger baselines we evaluate.

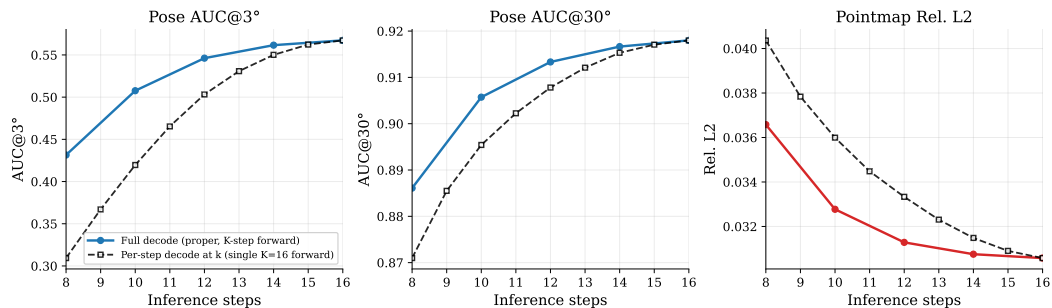


Figure 8: **Decoding intermediate results vs. using lower K_{inf} .** We compare using $K_{\text{inf}} < K_{\text{max}}$ steps explicitly to decoding \mathbf{z}_k at intermediate iterations k when $K_{\text{inf}} = K_{\text{max}}$, and show that explicitly conditioning the model on fewer iterations degrades performance less than early-stopping.

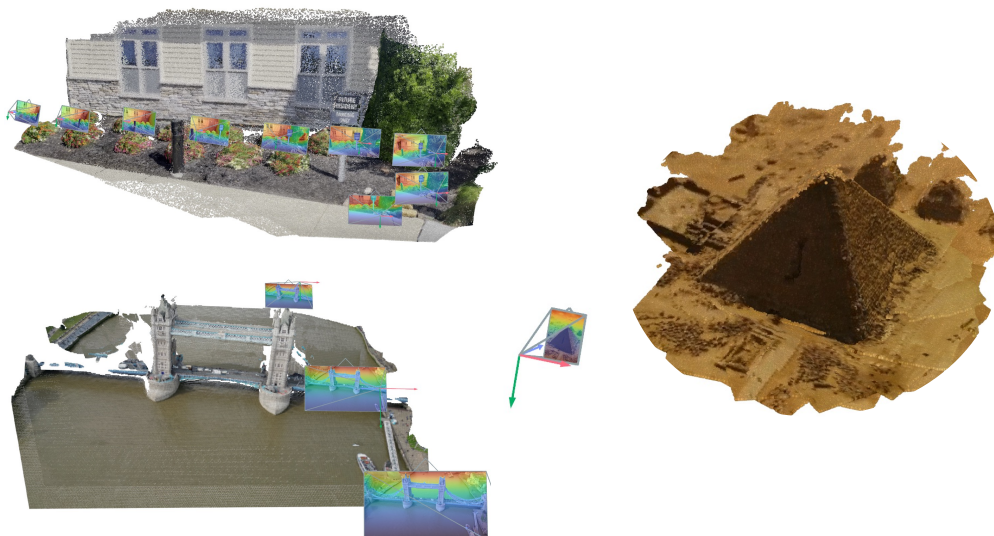


Figure 9: **Qualitative results.** Predicted point clouds and cameras for in-the-wild captures.